Nanotechnology

Photoluminescence of ZnO/ZnMgO heterostructure nanobelts grown by MBE

To cite this article before publication: Oscar Kennedy *et al* 2019 *Nanotechnology* in press https://doi.org/10.1088/1361-6528/ab60cb

Photoluminescence of ZnO/ZnMgO Heterostructure Nanobelts grown by MBE

Oscar W. Kennedy,[1] Maximilian Zapf,[2] Jean-Nicolas Audinot,[3] Soupitak Pal,[3] Santhana Eswara,[3] Tom Wirtz,[3] Carsten Ronning,[2] and Paul A. Warburton[1]

[1)] *London Centre for Nanotechnology, UCL, 17-19 Gordon Street, London, WC1H 0AH, UK*

[2)] *Institut für Festkörperphysik, Friedrich-Schiller-Universität Jena, Max-Wien-Platz 1, 07749 Jena, Germany*

[3)] *Materials Research and Technology Department, Luxembourg Institute of Science and Technology (LIST), Belvaux, Luxembourg*

ZnO nanobelts may grow with their polar axis perpendicular to growth direction. Appropriately heterostructured nanobelts therefore contain hetero-interfaces along the polar axis of ZnO where polarization mismatch may induce electron confinement. These interfaces run along the length of the nanobelts. Such heterostructure nanobelts are grown by molecular beam epitaxy and TEM images confirm the core-shell structure. The effects of shell-growth temperature on nano-heterostructures is investigated using photoluminescence and secondary ion mass spectrometry in a focussed ion-beam microscope with a Ne^+ as the primary ion beam. We perform low temperature photoluminescence on ensembles of such heterostructures and single nanostructure. We show how single nanobelts have photoluminescence spectra rich in features and attribute these to band misalignment at ZnO/ZnMgO interfaces embedded within nano-heterostructures.

I. INTRODUCTION

Heterostructures in one dimensional (1D) semiconducting nanostructures have been used to enhance their device-relevant properties. These advances include increases in electron mobility[1–3], improvement of optical properties[4] and embedding of functional devices such as p-i-n junctions within single nanowires[5]. They have also resulted in improvements to device functionality including ultrahigh responsivity photodetectors[6].

In 1D nano-heterostructures based on ZnO the combination of nanostructures with different crystallographic growth axes and different heterostructure geometries allow, in principle, the properties of these heterostructures to be engineered for functional properties. ZnO nanowires grow along the [0001] crystal axis and ZnO/ZnMgO core-shell and core-multi-shell heterostructures based on nanowires have previously been grown[7–9]. These heterostructured nanowires showed modified luminescence properties with luminescence peaks arising from both the quantum confined stark effect and quantum-well confinement. Other nanostructures of ZnO, such as ZnO nanobelts[10,11], grow along different crystal axes, including with [0001] perpendicular to the nanowire growth axis and different orientations where the polarization is oblique to the growth axis[12]. Therefore, in nanobelt core-shell structures the chemistry will be modulated along different crystal axes to that in nanowires.

This manuscript addresses embedding ZnO/ZnMgO heterointerfaces along the polar [0001] crystal axis which extends the length of the nanostructure. At this interface a two dimensional electron gas may form[13] due to the combination of polarisation and band-gap mismatch between the two materials. Polarization mismatched interfaces have previously been embedded into AlGaN/AlN/GaN nanowires[2] resulting in high mobility electrons confined at these heterointerfaces. Despite their promise for enhanced functional properties the only ZnO nanobelt heterostructures reported to date are biaxial ZnO/ZnS nanobelt heterostructures[14]. ZnO/ZnMgO heterostructure nanobelts have the device-relevant promise of allowing polarisation-mismatched heterointerfaces, and consequent high-mobility confined electrons, to extend the length of the 1D nanostructure. Additionally, surface strain relief common to 1D nanostructures may allow epitaxial strain occurring at the heterointerface to be relieved and the enhancement of properties beyond that found in planar geometries. Growing these structures by MBE allows for clean interfaces necessary for high mobility confined electrons and is the technique yielding the best results for these interfaces in thin-films[15].

In this manuscript we present the growth and investigation of ZnO/ZnMgO core-shell nanobelt heterostructures for the first time. TEM images show the core-shell structure on single nanobelts. We investigate the effects of shell-growth temperature on the resultant nanostructures by photoluminescence (PL) and secondary ion mass spectrometry (SIMS) in a focussed ion-beam (FIB) microscope with Ne^+ as the primary ion. PL performed on single nano-heterostructures at 4.2 K and show a rich variety of luminescence features.

II. EXPERIMENTAL

ZnO nanobelts were grown at 900°C on r-plane sapphire by gold-catalysed plasma assisted molecular beam epitaxy as described in Ref. 16. Nanobelt growth lasts for 90 mins with Zn beam equivalent pressure (BEP) of 4.2×10^{-7} mbar. After the nanobelt growth, the sample temperature was reduced to a shell growth temperature, Mg flux of $\sim 3\times10^{-8}$ mbar was introduced and ZnMgO

is grown for 30 mins. The Zn:Mg BEP fluctuates slightly from run to run due to small instabilities in the Mg source at low pressures.

Room temperature photoluminescence (PL) was performed using a Renishaw Fluorescence Microscope with excitation using a HeCd laser at 325nm. Single nanobelt PL was performed by dispersing nanobelts on a silicon substrate patterned with a grid of alignment marks, imaging the sample by SEM and mapping nanobelt locations to perform PL. Cryogenic PL was performed also using a HeCd-laser at 325 nm in a self-built P system and epifluorescence microscope with a 50× objective and numerical aperture of 0.42[17]. SIMS was performed on ensembles of heterostructure nanobelts using an ORION NanoFab helium ion microscope (HIM) (ZEISS Peabody, USA) equipped with a SIMS system (LIST, Luxembourg) specifically developed for the HIM[18,19]. Here we exploit the dual gas-source capability of the high-brightness gas field ion source equipping the HIM and use Ne^+ instead of He^+ as the primary ion beam. The advantage of using Ne^+ primary ions rather than He^+ ions for performing SIMS is given by the significantly higher sputter yield related to Ne^+ projectiles (due to their higher mass), resulting in increased SIMS count rates. SIMS is collected in two steps: first, electron images were registered by detecting the secondary electrons emitted from the sample surface scanned by a focused energetic Ne^+ ion beam (beam energy 20 keV, beam current 3 pA, matrix of 512x512 pixels, counting time per pixel of 50 s). Second, SIMS images were acquired using the Ne^+ beam (beam energy 20 keV, beam current 3 pA, matrix of 512x512 pixels, counting time per pixel of 2 ms). Bright field TEM was performed by first drop-casting nanobelts onto holey-carbon TEM grids before imaging in an FEI Tecnai G2 F20 TEM equipped with an energy dispersive spectroscopy (EDS) detector (Oxford Instruments) and a Fischione Model 3000 high angle annular dark field (HAADF) detector.

III. DISCUSSION

A. Ensemble Measurements

The effects of temperature on heterostructure growth were investigated by growing a series of samples varying the temperature of the shell growth from 500°C to 700°C. Room temperature PL spectra acquired on the samples are shown in Figure 1 together with a plain ZnO sample (i.e. no heterostructure growth) for reference.

The reference ZnO nanobelt sample has only one PL peak at 3.3 eV which is consistent with other reports for room temperature PL performed on ZnO nanostructures. The ZnO peak at 3.3 eV, caused by free-excitons near the band edge (NBE emission) is present for all other nanobelts even after ZnMgO side-wall growth showing that there is a pristine ZnO core present in the sample and that there is limited or no Mg-migration into the

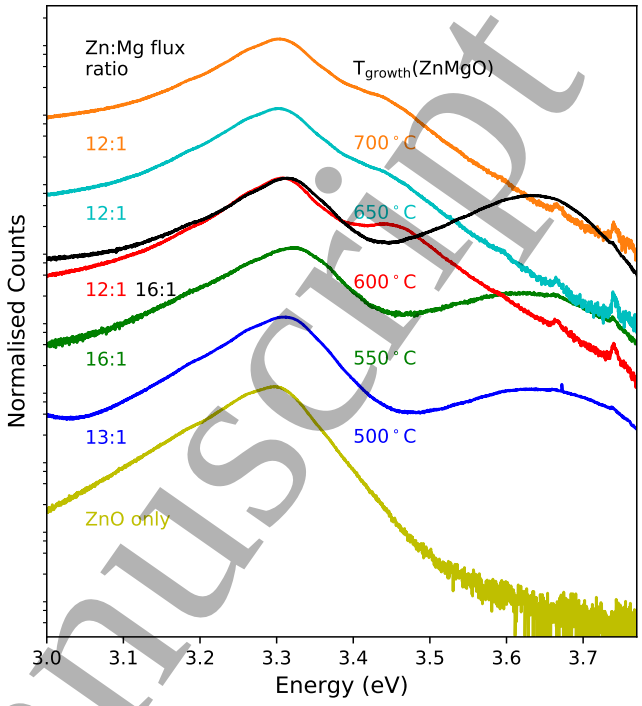

Figure 1. Room temperature ensemble PL performed on ZnO/ZnMgO nanobelt heterostructures where shell growth is performed at different temperatures and a plain ZnO nanobelt sample for reference. Spectra are normalised by their most intense emission, plot on logarithmic scales and offset for clarity. Two samples are grown with shell growth performed at 600°C and have no offset.

ZnO that would induce shifts of the PL peak[20]. Two samples were grown both with shell growth performed at 600°C and are plot in black and red in Figure 1. These are referred to as 600R (data plot in red in Figure 1) and 600B (data plot in black in Figure 1). Sharp peaks in Figure 1 at energies >3.6 eV are artefacts due to filtering of the pump laser.

For all heterostructure samples there is a clear PL signal at energies above the ZnO peak which is not present in the ZnO reference sample. These peaks are caused by the larger band-gap of ZnMgO and we observe that this luminescence peak shows a trend non-monotonic in shell-growth-temperature. For samples with shells grown 500°C, 550°C and 600B there is a broad PL peak centred at 3.63 eV. This peak becomes more intense relative to the ZnO peak with increasing shell growth temperature. The increase in intensity is likely due to the higher quality ZnMgO material deposited at a higher growth temperature. For the three samples; 600R and the samples with shell growth performed at 650°C and 700°C the ZnMgO peak is a shoulder on the ZnO peak at lower energy than that for the three samples discussed previously. This is particularly interesting for the two samples that were grown at 600°C which have different energy ZnMgO peaks. Sample 600R has a lower energy ZnMgO PL peak

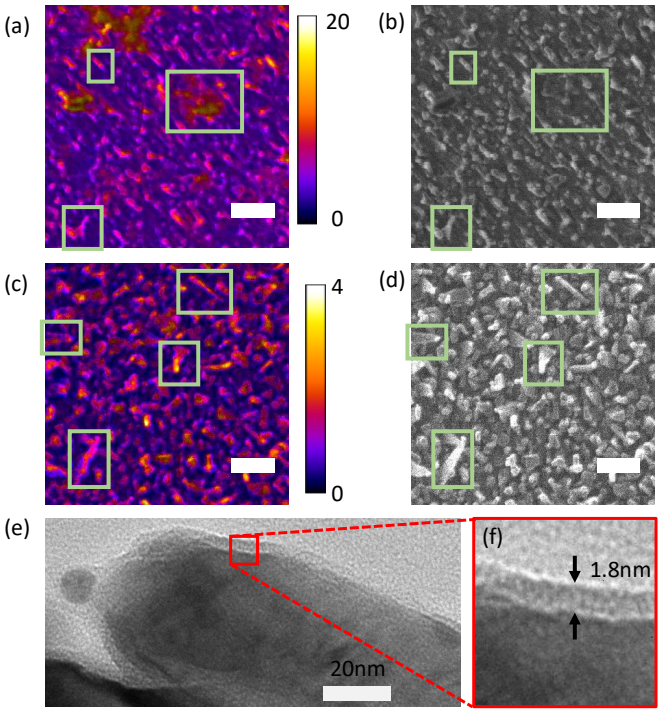

Figure 2. (a, c) Image fusion between SIMS map of Mg and secondary-electron image taken on the HIM with an integrated SIMS system using a raster-scanned Ne^+ ion beam. The colour-bars represent represent a Mg count intensity, comparable between (a) and (c) but given in arbitrary units; (b, d) the raw secondary-electron image of the same area performed on the sample with shell growth performed at 550°C (a, b) and 600R (c, d). Green boxes highlight the same region in the comparable image fusion and SE images. Scale bars in (a-d) are 500nm. (e) Bright field TEM imaging of a nanobelt from sample 600R showing the growth of a shell which is shown in close up in (f) where the shell is measured to be 1.8nm thick.

despite having a slightly higher fractional Mg pressure during shell growth. If the difference to PL peaks were due to fluctuations in the Mg flux the higher Mg flux should give a higher energy ZnMgO peak. We therefore believe that the difference between the two samples is due to fluctuations in growth temperature, where the noted temperature is only a set-point temperature. This shows that there is a cross-over in how heterostructures grow at ~600°C. The lower ZnMgO PL peak energy for samples with shells grown at higher energies shows that the Mg concentration in these samples is lower despite them actually having marginally higher fractional Mg fluxes. Zn has a lower boiling point than Mg meaning that at higher temperatures re-evaporation of adsorbed species should actually further increase the relative amount of Mg and thus the energy of the ZnMgO peak in contrast to the observation of a decrease in ZnMgO peak energy with shell growth temperature.

SIMS allows the Mg concentration to be mapped on an as-grown sample. This helps to interpret ensemble PL spectra as this shows the distribution of ZnMgO on the sample in the same configuration as the PL measurements are performed. SIMS was performed on two samples, the sample with shells grown at 550°C (Figure 2 a, b) and 600R (Figure 2 c, d). Using the intensity-hue-saturation technique[21], the high resolution secondary electron image and the SIMS map obtained both on the same instrument with the same Ne^+ primary ion beam are fused to correlate the elemental distribution with the topography (Figure 2 a, c). The high resolution secondary electron (SE) image is shown alongside the image fusion to clearly show the sample topography (Figure 2 b, d). Due to the high resolution SIMS map, low counts are collected (particularly from sample 600R), therefore a Gaussian blur of 2 pixel radius has been used to down-sample the SIMS data showing clearer variations in Mg concentration.

The sample with shells grown at 550 °C shows an increased Mg concentration on nanostructures relative to their surroundings as highlighted by the two smaller green boxes in Figure 2 (a, b). However, there are also large regions with higher Mg concentration which can not be correlated to any nanostructures, for instance the area in the large green box in Figure 2 (a, b). In contrast the same measurement performed on sample 600R shows increases in Mg concentration on nanostructures (highlighted by green boxes in Figure 2 (c, d)) and has no large regions of Mg concentration uncorrelated to nanostructures. The maximum Mg concentration, as determined by the maximum SIMS counts, in sample 600R is approximately 5 times lower than that in the sample with shells grown at 550 °C, consistent with the lower energy ZnMgO PL peak from these samples.

These SIMS measurements allow us to relate the change PL spectra at a shell-growth temperature of ~600 °C to how ZnMgO grows on the sample. At temperatures below this temperature ZnMgO grows both as shells on the nanostructures and in aggregates, uncorrelated to the nanostructures, on the sample. These aggregates are large and have larger Mg concentration than the ZnMgO on surrounding nanostructures shown by the higher count rate of secondary Mg ions. This ZnMgO dominates the PL signal originating from ZnMgO. At shell growth temperatures above 600°C Mg is no longer deposited in large aggregates on the sample surface and instead is deposited on the surfaces of nanostructures. PL spectra and SIMS maps show that the ZnMgO growing on the nanostructure's sidewalls has lower Mg concentration than that growing in aggregates on the sample. This may occur if the ZnMgO is growing epitaxially, as epitaxial matching may reduce the Mg incorporation due to effects such as strain. We conclude that growth of ZnO/ZnMgO nano-heterostructures should be performed with a shell growth temperature above 600 °C.

Bright field TEM (Figure 2 e,f) resolves 1.8 nm thick shells growing on single nanobelts. These images are taken with 0° tilt so that the electron beam is normal to the extended nanobelt face as shown schematically in

the SI. This imaging configuration means that TEM images show a projection of the nanostructure (which is approximately uniform in thickness) and confirms that there is ZnMgO growth on the polar sidewalls which is noteably the interface relevant for electron confiment. To confirm the core-shell structure EDS linescans were taken on a similar nanostructure and are shown in the SI. These linescans show that Mg is present in the middle of the nanostructure when viewed from this projection i.e. ZnMgO shells are present on all faces including the non-polar faces normal to the electron beam in this imaging configuration and not only on the sidewalls, confirming the core-shell structure.

In order to characterize the crystal quality of the different materials temperature dependent PL measurements were performed on ensembles of nanobelts with shells grown at 550°C (Figure 3 a) and sample 600R where the ZnMgO PL peak is a shoulder to the ZnO peak at room temperature (Figure 3 b). In both samples, as the temperature decreases, the ZnO peak narrows and shifts to higher energies caused by the Varshni-shift and the transition to donor bound excitons (DX). Furthermore, optical (LO) phonon replicas of the free exciton (FX) appear, two are present in sample 600R and three in the sample with shells grown at 550°C. The presence of LO phonon replicas is indicative of high crystal quality and therefore indicates higher quality ZnO in the sample with the lower shell growth temperature (see explanation below).

The broad ZnMgO PL peak in the sample with shells grown at 550°C is present at all measurement temperatures (including room temperature as shown in Figure 1). Its intensity relative to the ZnO peak increases slightly at lower temperatures but it remains a broad peak with no fine structure. This is consistent with the picture of random aggregates of ZnMgO from the SIMS data, where ZnMgO aggregates may have different Mg concentrations and have varying crystal quality.

In contrast the ZnMgO peak (arising from shells of heterostructures) for the sample 600R narrows and increases in energy with decreasing temperature. The ZnMgO peak remains broad relative to the ZnO peak even at 4 K, at which it has a central energy of ~3.49 eV. Despite being broaded than the ZnO peak, it has a well-defined energy implying a narrow spread in Mg concentration across the ZnMgO shells. The band-gap of $Zn_{1-x}Mg_xO$ has previously been determined to depend on the fractional Mg concentration as $E_g = 3.30 + 2.36 \times x$[22]. Assuming this relation can be approximately extrapolated to cryogenic temperatures (i.e. the Varshni shift isn't a function of Mg concentration), the shells in sample 600R have Mg concentration of $\sim 5\%$. If the width of the ZnMgO peak arises from a spread in the Mg concentration this corresponds to $\sim 1\%$ concentration fluctuations between shells of different nanostructures.

Below 100K a second peak between the ZnO and the ZnMgO appears. At 4K this second peak is located at ~3.44 eV. The 50 meV spacing between this peak and the ZnMgO peak is similar to the spacing between the D^0X and FX - LO peak for ZnO. As the LO phonon energy in ZnMgO is only a weak function of the fractional Mg concentration[23] this peak is determined to be a LO phonon replica of the free exciton in ZnMgO. The measurement of a LO phonon replica of the ZnMgO peak shows that the ZnMgO shells are of a high quality which supports the interpretation of epitaxial shell growth occurring at higher shell growth temperature. This may also explain the observation of the lower ZnO crystal quality in the sample with higher shell growth temperature as the growth of slightly epitaxially mismatched ZnMgO shells may strain the ZnO core.

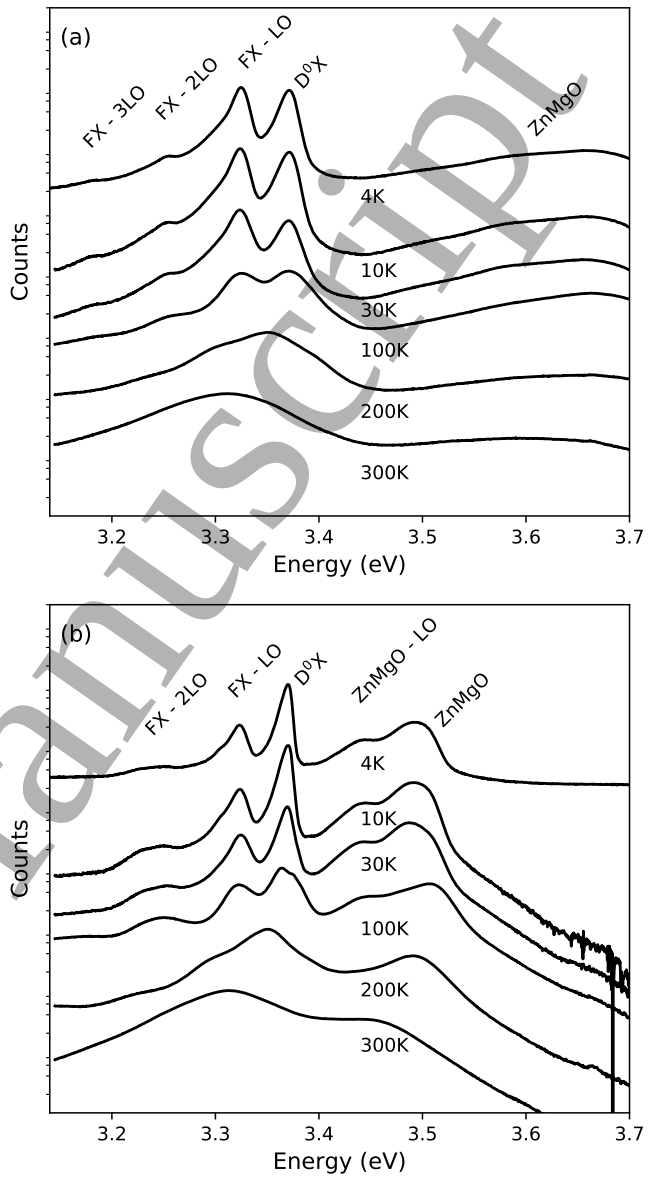

Figure 3. Temperature dependent ensemble PL measurements on (a) the sample with shells grown at 550°C and (b) 600R. Pump excitation has a power of 0.3 Wcm^{-2}.

B. Single Nanobelt Measurements

In order to characterize single nanobelts, nanobelts were dispersed onto Si substrates and PL was performed at 4K. SEM images of nanobelts dispersed on these grids are shown in the supplementary materials. Three such PL spectra from single nanobelts are shown in Figure 4.

Despite all nanobelts coming from the same sample, their individual PL spectra vary significantly. Whilst variation between nanostructures is expected from this randomly-nucleated growth technique, the variation in luminescence features is striking. All nanobelts show a peak from donor bound excitons in ZnO. However, even this peak varies between nanobelts. Nanobelt number two (NB2) has a peak, lacking fine structure and qualitativiely similar to the ensemble measurement in Figure 3 b. Both NB1 and NB3 show fine structure in this peak, including narrow, intense lines. The intense line in each of these samples has a width of only ∼1 meV and occurs at 3.369 eV for NB1, and 3.367 eV for NB3. The fine structure exists on top of a broad peak qualitatively similar to that in NB2 and the ensemble measurements. The small belt-to-belt variation explains why ensemble measurements show smooth peaks with no fine structure as the broad beam averages over many structures, blurring out details.

All nanobelts also have luminescence at energies above the ZnO band-gap with a peak centred at ∼3.48 eV. This lines up well with the relatively broad ZnMgO peak in ensemble measurements and is attributed to excitonic luminescence in ZnMgO. There is some spread in the central energy of this peak between the different nanobelts, implying that there is a spread in Mg concentration in the ZnMgO shells grown on these different nanostructures. The spread in central energy is similar to the breadth of the ZnMgO peak in ensemble measurements supporting the interpretation that the dominant peak broadening mechanism is concentration fluctuations between different nanobelts.

In addition to excitonic peaks the single-nanobelt-spectra include phonon replicas. NB1 has two phonon replicas of the free exciton of ZnO as in the ensemble measurements. NB2 also shows phonon replicas, however, the strongest phonon replicas for NB2 are of the donor bound exciton. In the ensemble measurements at 4K there is a low energy shoulder to the FX - LO peak which may be caused by D^0X - LO transitions, however the relatively low intensity of this peak indicates that this replica is not present in most nanobelts. In addition to D^0X peaks, NB2 has a weak FX - LO peak. NB3 has numerous peaks that approximately line up with the FX - LO peaks from NB1 and the D^0X - LO peaks from NB2.

In the PL spectra of single nanobelts there are additional peaks which are not be present in the ensemble measurements and cannot be explained by the luminescence properties of the virgin materials. NB1 has peaks at ∼3.42 eV and ∼3.46 eV, NB2 has a peak at 3.337 eV

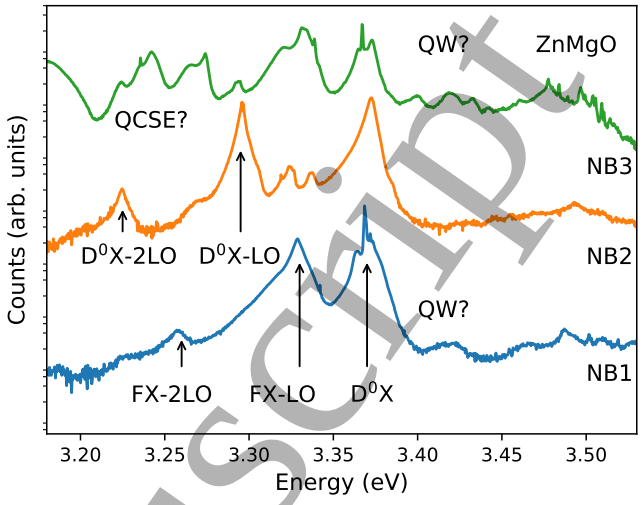

Figure 4. Single nanobelt PL spectra for nanobelts from 600R collected at 4K with a 3 μW excitation power. Spectra are normalised to the D^0X peak, offset for clarity and plot with logarithmic counts. The excitation pump has a power density of 95 Wcm^{-2}. Where the origin of the peak is known it is labelled, other peaks are marked by suggested causes.

and the rich spectrum of NB3 has a multitude of these peaks from the lowest energies collected up to 3.44 eV, just below the PL peak from the ZnMgO. While these PL peaks can not be explained by the virgin materials, they occur at energies where luminescence arising due to quantum confinement at interfaces is expected to occur.

The interfaces in these nanostructures may have a variety of band misalignments due to the combination of band-gap mismatch and polarization mismatch along different crystal axes. Solving Poisson's equation shows that along the c-axis [0001], the polarization mismatch and band mismatch have an additive effect, contributing to the same band-offset, along $[000\bar{1}]$ the polarization and band-gap mismatch counteract one another, whilst in non-polar interfaces there is only a band-offset[24]. All of these interfaces may occur simultaneously within the same heterostructured nanobelt. This is in addition to modifications to band structure from the nanobelt surface such as surface band bending[25]. This explains why PL spectra may be so rich in features and means that definitively interpreting these spectra is extremely challenging.

In order to understand these spectra we consider two additional luminescence processes which may occur at interfaces with band and polarization mismatches and which have previously been observed in ZnO/ZnMgO nanowire heterostructures[8]. These are the quantum confined Stark effect (QCSE) which results in below-gap luminescence and quantum well luminescence which results in above-gap luminescence. In NB1 there is a peak at 3.42 eV and in NB3 there are peaks at 3.40 eV, 3.42 eV and 3.43 eV all of which occur at energies compatible

with being caused by quantum well confinement. Likewise the multiple peaks below the ZnO band-gap for NB3 are consistent in energy and intensity with being caused by QCSE with reports of QCSE luminescence at the same interface occurring from 140meV[7] to 40meV[26] below the ZnO peak. Whilst interpreting all details of these spectra remains challenging, they provide some evidence of quantum confinement in these nanobelt heterostructures.

IV. CONCLUSIONS

We have grown ZnO/ZnMgO core-shell nanobelt heterostructures by molecular beam epitaxy as confirmed by bright-field TEM images. Room temperature PL collected on samples as a function of the ZnMgO shell-growth-temperature show non-monotonic changes in central energy and intensity of the ZnMgO PL peak. This implies a cross-over temperature for shell-growth dynamics. The change in growth modes is supported by high-resolution SIMS imaging obtained with a highly focussed Ne^+ ion beam performed on ensembles of nanoheterostructures showing ZnMgO preferentially growing on nanostructures at higher temperatures and both growing on nanostructures and aggregating in large regions at lower growth temperatures.

We perform cryogenic PL on ensembles of nanostructures and single nanostructures showing evidence of good crystalline quality and luminescence features from single nanostructures. Some of these PL features aren't explained by virgin material properties and are indicative of quantum confinement at ZnO/ZnMgO interfaces. These heterostructures hold promise for future devices where high mobility electrons are embedded within quasi 1D nanostructures and stretch along the long axis of these nanostructures.

V. ACKNOWLEDGEMENTS

The authors gratefully acknowledge financial support from EPSRC grant reference EP/H005544/1 (PAW and OWK), EP/P510270/1 (OWK) and Deutsche Forschungsgemeinschaft via grant FOR1616 (MZ and CR). OWK acknowledges the PicoFIB network, supported by the Leverhulme Trust, for funding a research exchange visit.

REFERENCES

[1] Jessica L Boland, Sonia Conesa-Boj, Patrick Parkinson, Gozde Tutuncuoglu, Federico Matteini, Daniel Ruffer, Alberto Casadei, Francesca Amaduzzi, Fauzia Jabeen, Christopher L Davies, Hannah J Joyce, Laura M Herz, Anna Fontcuberta i Morral, and Michael B Johnston. Modulation doping of GaAs/AlGaAs core–shell nanowires with effective defect passivation and high electron mobility. *Nano Letters*, 15(2):1336–1342, 2015.

[2] Yat Li, Jie Xiang, Fang Qian, Silvija Gradecak, Yue Wu, Hao Yan, Douglas A Blom, and Charles M Lieber. Dopant-free GaN/AlN/AlGaN radial nanowire heterostructures as high electron mobility transistors. *Nano Letters*, 6(7):1468–1473, 2006.

[3] S Conesa-Boj, A Li, S Koelling, M Brauns, J Ridderbos, TT Nguyen, MA Verheijen, PM Koenraad, FA Zwanenburg, and Erik PAM Bakkers. Boosting Hole Mobility in Coherently Strained [110]-Oriented Ge–Si Core–Shell Nanowires. *Nano Letters*, 17(4):2259–2264, 2017.

[4] Cheol Hyoun Ahn, Sanjay Kumar Mohanta, Bo Hyun Kong, and Hyung Koun Cho. Enhancement of band-edge emission of ZnO from one-dimensional ZnO/MgZnO core/shell nanostructures. *Journal of Physics D: Applied Physics*, 42(11):115106, 2009.

[5] Thomas J Kempa, Bozhi Tian, Dong Rip Kim, Jinsong Hu, Xiaolin Zheng, and Charles M Lieber. Single and tandem axial pin nanowire photovoltaic devices. *Nano Letters*, 8(10):3456–3460, 2008.

[6] Bin Zhao, Fei Wang, Hongyu Chen, Lingxia Zheng, Longxing Su, Dongxu Zhao, and Xiaosheng Fang. An Ultrahigh Responsivity ($9.7\ mAW^{-1}$) Self-Powered Solar-Blind Photodetector Based on Individual ZnO–Ga2O3 Heterostructures. *Advanced Functional Materials*, 27(17):1700264, 2017.

[7] Robin Thierry, Guillaume Perillat-Merceroz, Pierre-Henri Jouneau, Pierre Ferret, and Guy Feuillet. Core–shell multi-quantum wells in ZnO/ZnMgO nanowires with high optical efficiency at room temperature. *Nanotechnology*, 23(8):085705, 2012.

[8] BQ Cao, J Zúñiga-Pérez, N Boukos, C Czekalla, H Hilmer, J Lenzner, A Travlos, M Lorenz, and M Grundmann. Homogeneous core/shell ZnO/ZnMgO quantum well heterostructures on vertical ZnO nanowires. *Nanotechnology*, 20(30):305701, 2009.

[9] Bo Hyun Kong, Sanjay Kumar Mohanta, Young Yi Kim, and Hyung Koun Cho. Synthesis and characterization of ZnO/MgZnO heterostructure nanorods by simple two-step evaporation. *Nanotechnology*, 19(8):085607, 2008.

[10] Zheng Wei Pan, Zu Rong Dai, and Zhong Lin Wang. Nanobelts of semiconducting oxides. *Science*, 291(5510):1947–1949, 2001.

[11] Xiang Yang Kong and Zhong Lin Wang. Polar-surface dominated ZnO nanobelts and the electrostatic energy induced nanohelixes, nanosprings, and nanospirals. *Applied Physics Letters*, 84(6):975–977, 2004.

[12] Wen-Zhong Wang, Bao-Qing Zeng, Jian Yang, Bed Poudel, JY Huang, Michael J Naughton, and ZF Ren. Aligned ultralong zno nanobelts and their enhanced field emission. *Advanced Materials*, 18(24):3275–3278, 2006.

[13] H Tampo, H Shibata, K Maejima, A Yamada, K Matsubara, P Fons, S Kashiwaya, S Niki, Y Chiba, T Wakamatsu, et al. Polarization-induced two-dimensional electron gases in ZnMgO/ZnO heterostructures. *Applied Physics Letters*, 93(20):202104, 2008.

[14] Jian Yan, Xiaosheng Fang, Lide Zhang, Yoshio Bando, Ujjal K Gautam, Benjamin Dierre, Takashi Sekiguchi, and Dmitri Golberg. Structure and cathodoluminescence of individual ZnS/ZnO biaxial nanobelt heterostructures. *Nano Letters*, 8(9):2794–2799, 2008.

[15] Joseph Falson, Yusuke Kozuka, Masaki Uchida, Jurgen H Smet, Taka-hisa Arima, Atsushi Tsukazaki, and Masashi Kawasaki. MgZnO/ZnO heterostructures with electron mobility exceeding $1\times\ 10^6\ cm^2/Vs$. *Scientific Reports*, 6:26598, 2016.

[16] Oscar W Kennedy, Maddison L Coke, Edward R White, Milo SP Shaffer, and Paul A Warburton. MBE growth and morphology control of ZnO nanobelts with polar axis perpendicular to growth direction. *Materials Letters*, 212:51–53, 2018.

[17] Sebastian Geburt. *Lasing and ion beam doping of semiconductor nanowires*. PhD thesis, 2013.

[18] D Dowsett and T Wirtz. Co-registered in situ secondary electron and mass spectral imaging on the helium ion microscope demonstrated using lithium titanate and magnesium oxide nanoparticles. *Analytical Chemistry*, 89(17):8957–8965, 2017.

[19]Tom Wirtz, Olivier De Castro, Jean-Nicolas Audinot, and Patrick Philipp. Imaging and Analytics on the Helium Ion Microscope. *Annual Review of Analytical Chemistry*, 12, 2019.

[20]OW Kennedy, ER White, MSP Shaffer, and PA Warburton. Vapour-liquid-solid growth of ZnO-ZnMgO core–shell nanowires by gold-catalysed molecular beam epitaxy. *Nanotechnology*, 30(19):194001, 2019.

[21]Florian Vollnhals, Jean-Nicolas Audinot, Tom Wirtz, Muriel Mercier-Bonin, Isabelle Fourquaux, Birgit Schroeppel, Udo Kraushaar, Varda Lev-Ram, Mark H Ellisman, and Santhana Eswara. Correlative microscopy combining secondary ion mass spectrometry and electron microscopy: comparison of intensity–hue–saturation and laplacian pyramid methods for image fusion. *Analytical Chemistry*, 89(20):10702–10710, 2017.

[22]A Ohtomo, M Kawasaki, T Koida, K Masubuchi, H Koinuma, Y Sakurai, Yasuda Yoshida, T Yasuda, and Y Segawa. Mg_xZn_{1-x} O as a II–VI widegap semiconductor alloy. *Applied Physics Letters*, 72(19):2466–2468, 1998.

[23]C Bundesmann, A Rahm, M Lorenz, M Grundmann, and Mathias Schubert. Infrared optical properties of Mg_xZn_{1-x} O thin films ($0 \leq x \leq 1$): Long-wavelength optical phonons and dielectric constants. *Journal of Applied Physics*, 99(11):113504, 2006.

[24]Oscar W Kennedy. *MBE-grown ZnO-based nanostructures for electronics applications*. PhD thesis, 2019.

[25]Afsoon Soudi, Cheng-Han Hsu, and Yi Gu. Diameter-dependent surface photovoltage and surface state density in single semiconductor nanowires. *Nano Letters*, 12(10):5111–5116, 2012.

[26]T Makino, A Ohtomo, CH Chia, Y Segawa, H Koinuma, and M Kawasaki. Internal electric field effect on luminescence properties of ZnO/(Mg, Zn) O quantum wells. *Physica E: Low-dimensional Systems and Nanostructures*, 21(2-4):671–675, 2004.